



## An Investigation on the Electrodeposition Mechanism of Ni-TiO<sub>2</sub> Nanocomposite Coatings

Soha Mohajeri<sup>1</sup>, Abolghassem Dolati<sup>1</sup>, Mohammad Ghorbani<sup>1</sup>

<sup>1</sup>Department of Materials Science and Engineering, Sharif University of Technology, Tehran, Iran.

Received: 9 August 2016; Accepted: 10 October 2016

Corresponding author email: [smohajeri@alum.sharif.edu](mailto:smohajeri@alum.sharif.edu)

### ABSTRACT

In this research, a sol-modified composite electrodeposition technique that combines the sol-gel method with the conventional electrodeposition process was utilized to deposit Ni-TiO<sub>2</sub> nanocomposite coatings. Cyclic voltammetry and chronoamperometry techniques were applied to study the influence of the TiO<sub>2</sub> sol concentration on the deposits' electrochemical behavior. The results clearly showed that for higher sol concentrations, the onset potential of the nanocomposite deposition decreased compared to that of the pure Ni. The Scharifker-Hill model was utilized at the initial times of deposition to study the nucleation mechanism. It was demonstrated that the nucleation mechanism of the nanocomposite at low overpotentials followed the progressive system, whereas at higher overpotentials it was found to be instantaneous with the three-dimensional growth mechanism. The weight percentages of the codeposited TiO<sub>2</sub> nanoparticles were measured, and according to the results, the higher sol concentrations in the plating bath led to a higher TiO<sub>2</sub> nanoparticle content. The XRD results confirmed the presence of the anatase phase in the Ni-TiO<sub>2</sub> nanocomposite coatings after 3 hours of heat treatment at 450°C. The surface morphology was studied by the scanning electron microscopy, confirming that the addition of higher sol concentrations refined the microstructure, particularly under higher deposition overpotentials. This was attributed to increased nucleation sites and the slow growth rate of the nuclei.

**Keywords:** Electrodeposition; Ni-TiO<sub>2</sub>; Nanocomposite; Mechanism.

---

How to cite this article:

Mohajeri S, Dolati A, Ghorbani M. An Investigation on the Electrodeposition Mechanism of Ni-TiO<sub>2</sub> Nanocomposite Coatings.

*J Ultrafine Grained Nanostruct Mater*, 2016; 49(2):51-63.

DOI: [10.7508/jufgnsn.2016.02.01](https://doi.org/10.7508/jufgnsn.2016.02.01)

### 1. Introduction

With the increasing availability of nanoparticles in recent years, the interest in nanoparticle strengthened dispersion layers has grown [1, 2]. Much attention has been focused on the development of ceramic/metal nanocomposite coatings, since such materials offer outstanding mechanical and multifunctional properties [3, 4]. Nanocomposite coatings offer various benefits, such as high levels of wear and oxidation resistance, high-temperature corrosion protection, and

self-lubrication to the deposited surface [5, 6]. However, these properties mainly depend upon both the matrix phases of the composite coating and the amount and distribution of the codeposited particles; these aspects are related to many process parameters, including particle characteristics, electrolyte composition, and the applied current mode (direct current or pulsed current) [7]. Nanoparticles at the grain boundaries prevent dislocation movements and recrystallization procedures at elevated temperatures. Therefore,

microhardness and thermal stability increase markedly. The improved wear resistance results mainly from the fine crystalline microstructure, as well as the increased microhardness [8].

Composite electrodeposition technology is one of the methods used to fabricate the metal matrix composite coatings. The basic process is conducted in the composite electrodeposition solution in which a large amount of insoluble powder is suspended by stirring. The powder is embedded into the coating during the direct current (DC) electrodeposition of the metal matrix. Since nanoparticles possess high surface energy, it would normally be difficult to disperse them in the suspension. Although agitation and surfactants can diminish the agglomeration of the powder, their effects are limited [9]. There is, however, a novel sol-enhanced composite electrodeposition technique that combines the sol-gel method with traditional electrodeposition [10]. In the conventional sol-gel method, the nucleation and growth rates of the film are controlled by the sol characteristics [11]. Conversely, the sol-modified electrodeposition technique benefits from the advantages of both the electrodeposition and sol-gel methods. Since the potential, as well as the sol concentration in the bath, govern the rate of deposition and the composition of the deposited film, the control of the codeposition process is very high [12].

The electrodeposition of nickel has historically been a major subject of electrochemical research, due to its enormously useful properties and performance characteristics. Most research has been focused on the mechanism and properties of Ni electrodeposits obtained from sulfate or sulfate-chloride electrolytes, with a special emphasis on Watts baths [13-15]. With regards to the generally agreed upon mechanism, it has been clarified that in sulfate electrolytes, the hydrogen evolution reaction (HER) occurs prior to nickel deposition, leading to a diffusion-controlled reduction at low overpotentials [16]. However, it has been proven that the deposition process in the Watts bath begins with nickel reduction, because chloride anions are preferentially adsorbed on the surface in competition with protons. Therefore, at low overpotentials, the nickel electrodeposition from the Watts solution containing a high nickel concentration is charge-transfer controlled [17].

Recently, special attention has been paid to the oxides of transitional metals; among them, titanium dioxide is believed to be one of the most promising

[18, 19].  $\text{TiO}_2$  has various applications, including water splitting, environmental purification, self-cleaning coatings, sensors, solar cells, photocatalysis, and disinfection [20-22]. In composite materials, the  $\text{TiO}_2$  phase, with its high strength and hardness, can serve as an effective reinforcement to fortify the composite and increase hardness and wear resistance [23]. Ni matrix composites reinforced by  $\text{TiO}_2$  nanoparticles exhibit interesting photoelectrochemical and photocatalytic behaviors [24-26], as well as improved mechanical properties [27]. The microhardness and wear resistance of sol-enhanced Ni- $\text{TiO}_2$  nanocomposite coatings are significantly improved and have much smoother surfaces, which can improve corrosion resistance [28].

In the present study, Ni- $\text{TiO}_2$  nanocomposite coatings were deposited on copper substrates by a direct current electrodeposition process. The electrodeposition mechanism of the Ni- $\text{TiO}_2$  coating was studied via electrochemical techniques. The nucleation and growth mechanisms were characterized, and the effects of sol concentrations on the composition and microstructure of the deposits were studied.

## 2. Experimental

To obtain 100 mL of  $\text{TiO}_2$  sol, 18.5 mL of titanium tetraisopropoxide (TTIP) with a purity of 97% was dissolved in 78.5 mL of ethanol and stirred at room temperature for 30 minutes. This solution was added drop-wise to 4 mL of a water-acid mixture (pH = 1-2) and continuously stirred. A transparent yellow sol was obtained after 24 hours of aging. Different amounts of sol were mixed in the Watts bath, and the deposition was performed immediately thereafter. Simultaneously, the solution was magnetically stirred by a thermostat-heating magnetic stirrer at a rate of 150 r/min, in order to prevent sedimentation. The compositions of the electroplating baths are shown in Table 1. For comparison purposes, the pure Ni coating without the addition of the  $\text{TiO}_2$  sol was also deposited, with similar bath composition and plating conditions. The anode was a 5 cm × 2 cm pure Ni plate, and 2 cm × 1 cm copper plates were used as substrates. Specimens were mechanically polished to a 1,200 grit finish with SiC papers, and pre-treated prior to the electrodeposition by immersing them in acetone for 10 minutes. The potential was recorded with respect to the saturated calomel electrode (SCE) during the deposition process. Electrochemical

experiments, including those employing cyclic voltammetry and chronoamperometry techniques, were carried out via an EG&G PAR potentiostat model 273A. The cyclic voltammetry curves were utilized to understand the mechanism of the Ni deposition at scan rates of 20 to 100 mV/sec, and the effects of different concentrations of TiO<sub>2</sub> sol on the electrodeposition process were investigated. The chronoamperometry curves were recorded within the potential range of -600 to -900 mV vs. SCE for 250 seconds. The Scharifker-Hill model was utilized at the initial times of deposition to study the nucleation mechanism. In order to standardize the comparison, the thicknesses of all of the coatings were controlled by the plating time to be approximately ~14µm, for a specific deposition potential. Finally, the coatings were annealed at 450°C for 3 hours to facilitate the formation of anhydrous nanocrystalline TiO<sub>2</sub>.

In order to measure the weight percentages of the codeposited TiO<sub>2</sub> nanoparticles, the substrates were weighed before and after deposition, and the weights of the coatings were obtained. Afterwards, the Ni-TiO<sub>2</sub> composite coatings were dissolved in an HNO<sub>3</sub> solution. Since TiO<sub>2</sub> particles do not react with HNO<sub>3</sub>, they precipitated in the solution. The obtained solutions were kept for two weeks and processed with a centrifuge so that the TiO<sub>2</sub> nanoparticles precipitated completely. Then, the TiO<sub>2</sub> particles were separated and dried at 90°C for 20 hours. These particles were weighed with a high-precision microbalance, and the weight percentages of the TiO<sub>2</sub> particles in the coatings were calculated with an accuracy of ±0.01 wt.%. The phase structures of the separated TiO<sub>2</sub> nanoparticles and the annealed coatings were verified by X-ray diffraction (XRD). A transmission electron

microscopy (TEM) investigation of the separated TiO<sub>2</sub> nanoparticles was performed using a ZEISS TEM model EM-10C operating at 100 kV. The surface morphology of the coatings was studied using a scanning electron microscopy (SEM); via this method, the thicknesses of the coatings were also determined.

### 3. Results and discussion

In order to evaluate the deposition of Ni<sup>2+</sup> ions in the range of E<sub>OCP</sub> = -200 to the vertex potential of -1000 mV vs. SCE, the Watts bath (see Table 1) was prepared without the addition of the TiO<sub>2</sub> sol, and voltammetry tests were carried out at various scan rates (20, 50, 100 mV/sec). Fig. 1(a) demonstrates the cyclic voltammetry curves in the solution without the addition of TiO<sub>2</sub> sol for these scan rates. This potential range was chosen to avoid oxygen or hydrogen evolution. The kinetics of the nickel electrodeposition from the Watts bath is carried out by one adsorption and two electrochemical reactions, as follows [29]:



where the rate-determining step is Reaction

Table 1- Composition of electrodeposition baths and processing parameters

Composition and parameters	Value
NiSO <sub>4</sub>	0.005 M
NiCl <sub>2</sub>	0.3 M
H <sub>3</sub> BO <sub>3</sub>	0.48 M
TiO <sub>2</sub> sol	10, 15, 20 and 25 mL/L
Sodium dodecyl sulphate (SDS)	0.005 g/L
pH	4±0.2
Temperature	50°C
Magnetic stirring speed	150 rpm

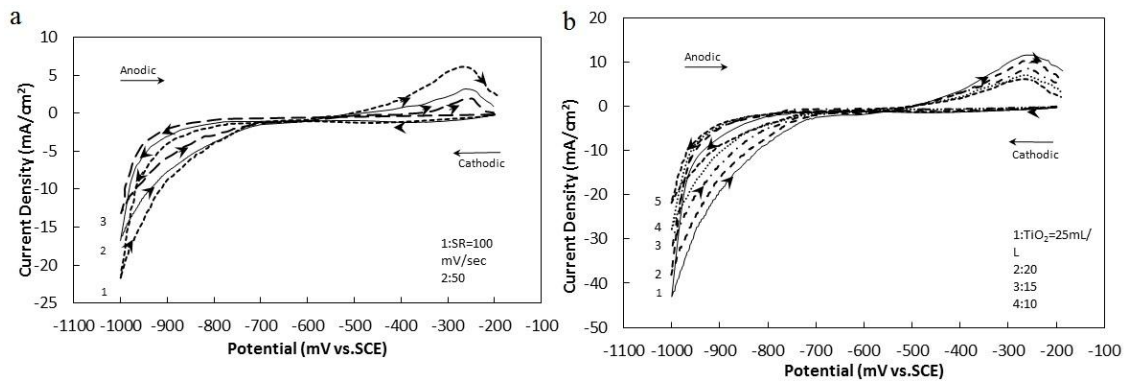
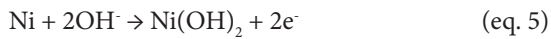


Fig. 1- Cyclic voltammetry curves in the Watts bath (a) without the addition of TiO<sub>2</sub> sol at various scan rates (20, 50, 100 mV/sec), and (b) with the addition of different concentrations of TiO<sub>2</sub> sol (0, 10, 15, 20, 25 mL/L) at a scan rate of 100 mV/sec.

(2) (i.e., the first-electron transfer step) [29]. Accordingly, the formation of the  $\text{NiOH}^+$  intermediate species precedes the charge transfer step that controls the Ni nucleation process (i.e., that represents the rate-limiting step). An excess of  $\text{H}^+$  ions (at  $\text{pH} < 5$ ) destabilizes the intermediate  $\text{NiOH}^+$  species; thus, the adsorption of the  $\text{NiOH}_{\text{ads}}^+$  is slow and the reduction of the  $\text{Ni}^{2+}$  ions is under the charge transfer control [30] (see Fig. 1(a)). From these data, it can be seen that with an increase of the potential in the cathodic direction at a scan rate of 20 mV/sec, the current density of the Ni deposition begins to increase at approximately -800 mV vs. SCE. As the scan rate increases to 100 mV/sec, the onset potential of the Ni electroplating shifts to -780 mV vs. SCE, revealing the influence of the scan rate on the deposition potential. The electron transfer coefficient ( $\alpha$ ) can be obtained from the cyclic voltammogram using the Tafel equation [31]; for the scan rates of 20, 50, and 100 mV/sec,  $\alpha$  is estimated to be 0.18, 0.19, and 0.21, respectively. Therefore, higher scan rates are found to increase the reduction rate of the  $\text{Ni}^{2+}$  ions. After the scan direction is reversed, the voltammograms contain anodic peaks of about -250 mV for all scan rates. These peaks correspond to the oxidation of the cathodically-deposited nickel through the following reactions [32]:



and/ or



The formation of the  $\text{HNiO}_2^-$  species is considered as the starting point for the dissolution process. It is assumed that the initial dissolution rate of the Ni, in the form of  $\text{HNiO}_2^-$  (Reaction 4), continues at a rate equal to that of the hydroxide film formation (the oxidation of the Ni to  $\text{Ni}(\text{OH})_2$ , Reaction 5). As the potential is swept further in the anodic direction, the rate of the nickel hydroxide formation exceeds the dissolution rate of the nickel. At this stage, the metal is passivated by the presence of the  $\text{Ni}(\text{OH})_2$  on its surface, and further oxidation cannot easily take place. Therefore, the anodic current decreases after the peak [32].

In order to evaluate the effects of the  $\text{TiO}_2$  sols of various concentrations on the electrochemical behavior of the Ni- $\text{TiO}_2$  deposition, Watts solutions with and without different amounts of the  $\text{TiO}_2$  sol were selected, and the voltammetry curves were plotted at a scan rate of 100 mV/sec. Fig. 1(b)

reveals that the presence of the  $\text{TiO}_2$  sol in the Watts bath results in an increase of the deposition current densities, and the curves shift toward more positive potentials. This can be attributed to an increase in the surface area of the cathode, due to the adsorbed semi-conductive  $\text{TiO}_2$  nanoparticles that provide more nucleation sites for the nickel deposition; therefore, the reduction of  $\text{Ni}^{2+}$  ions is carried out with less energy [12]. Additionally, according to Whithers' theory [33], the  $\text{TiO}_2$  nanoparticles can adsorb the hydrated Ni ions in the electrolyte, followed by a powerful transportation to the cathode surface under the effect of the electrical field. On the cathode surface, these nanoparticles increase the area available for mass flux and facilitate the electric discharge of  $\text{Ni}^{2+}$  ions, leading to an increase in the current density. As shown in Fig. 1(b), with the addition of different amounts of  $\text{TiO}_2$  sol to the solution, the deposition potential of the Ni shifts from -780 mV vs. SCE to less negative values; for 25 mL/L of  $\text{TiO}_2$  sol, it reaches -750 mV vs. SCE. Moreover, the addition of the  $\text{TiO}_2$  sol increases the anodic peak's current density. This behavior is due to the fact that the codeposition of the  $\text{TiO}_2$  particles refines the nickel crystallites [23], and thus a higher active surface area is subjected to the dissolution potential. Furthermore, the possible micro-galvanic cells between the  $\text{TiO}_2$  particles and nickel grains can also enhance the nickel dissolution [12].

The electrodeposition mechanisms of the Ni and Ni- $\text{TiO}_2$  electrodeposits were studied via a chronoamperometric analysis. Fig. 2 illustrates the *i-t* curves for the Watts solutions with and without the addition of different concentrations of  $\text{TiO}_2$  sol, under the deposition potentials of -600, -700, -800 and -900 mV vs. SCE for 250 seconds. The *i-t* transients have a common dependence on the applied potential, whereas with an increase in the cathodic overpotential, the current density increases as well. At low overpotentials, the current density decreases rapidly without any considerable nucleation process, due to the double layer capacitance (see Figs. 2(a) and (b)). In Figs. 2(c) and (d), the applied potentials are more cathodic than the potentials at which the initial deposition of the pure nickel (-780 mV vs. SCE) and Ni- $\text{TiO}_2$  nanocomposites containing different amounts of  $\text{TiO}_2$  (-770 to -750 mV vs. SCE) occur. The curves show significant peaks, followed by pronounced falls to stationary current densities. Based on the characteristic shape of the chronoamperometry

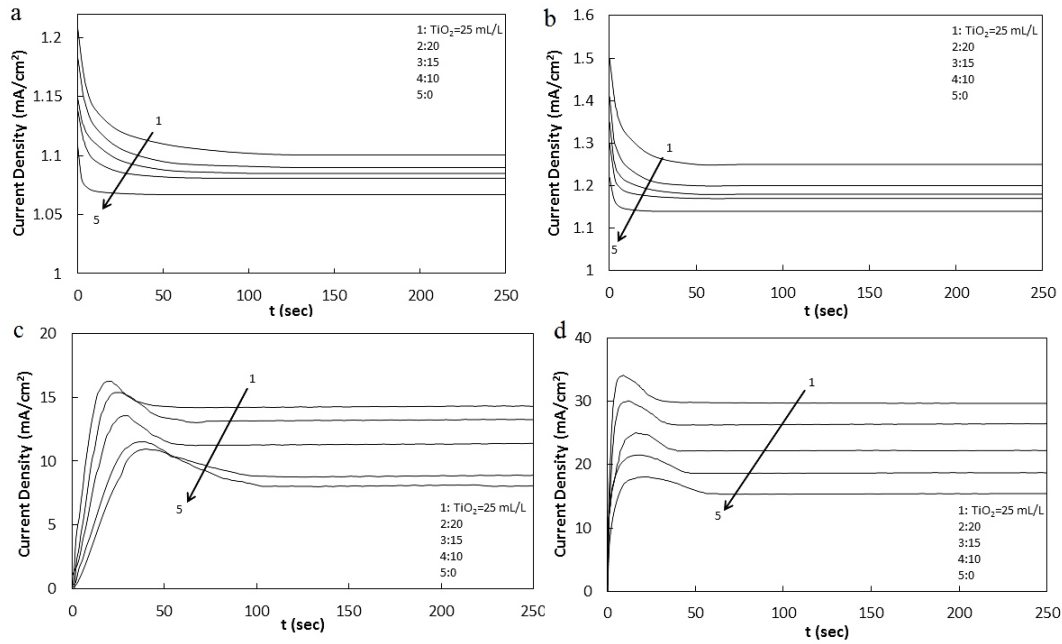


Fig. 2- Chronoamperometry curves for deposition in the Watts bath with and without the addition of different concentrations of  $\text{TiO}_2$  sol, under the deposition potentials of (a) -600, (b) -700, (c) -800, and (d) -900 mV vs. SCE.

curves, it seems that a nucleation and growth mechanism can describe the electrodeposition process, and the rate of growth is limited by diffusion. Actually, at the initial times, the current density increases due to the nucleation process and 3D growth of the nuclei [34]. Afterwards, the current drops and deposition is controlled by diffusion. This might be due to the coevolution of hydrogen, which interrupts the nickel nucleation [35]. It is obvious that at a constant deposition potential, the  $i$ - $t$  transients are dependent upon the  $\text{TiO}_2$  sol concentration; increasing the sol concentration causes the initial peak of current density to also increase. It should be noted that although the  $\text{TiO}_2$  nanoparticles are semi-conductive and cannot enhance the charge transfer in the solution, higher sol concentrations lead to higher incorporation of the  $\text{TiO}_2$  nanoparticles [12]. Correspondingly, the cathode surface area is increased and the electric discharge of the  $\text{Ni}^{2+}$  ions is facilitated, leading to an increase in the current density. Moreover, the  $\text{TiO}_2$  nanoparticles provide more nucleation sites for the deposition of the  $\text{Ni}^{2+}$  ions, and accelerate the nucleation process. Thus, the critical time for the nucleation decreases. A comparison of Figs. 2(c) and (d) reveals that as the deposition potentials shift toward more cathodic values, the sharp drop in the current density occurs earlier and the relaxation time decreases, resulting

in a more rapid nucleation of nickel deposits. This can alter the electrodeposition mechanism.

In order to verify the nucleation and growth mechanisms of the Ni and Ni- $\text{TiO}_2$  composites for different  $\text{TiO}_2$  sol concentrations under various overpotentials, the Scharifker-Hill model was applied to the  $i$ - $t$  transients (see Figs. 2(c) and (d)). This model allows for the type of nucleation to be determined via an analysis of the chronoamperograms prior to the overlap of the nuclei diffusion zones. At this stage, the reduction of hydrogen ions is not prominent, and a majority of the current corresponds to a reduction of nickel ions [36]. According to this model, instantaneous nucleation takes place when the growth of nuclei occurs slowly during the initial time of deposition. On the other hand, progressive nucleation occurs when the rate of new nuclei formation arises over longer periods of time, and the nuclei grow rapidly. The instantaneous and progressive nucleations are shown in Equations (6) and (7), respectively:

$$\frac{i^2}{i_m^2} = \frac{1.9542}{t} \left\{ 1 - \exp \left[ -1.2564 \left( \frac{t}{t_m} \right) \right] \right\} \quad (\text{eq. 6})$$

$$\frac{i^2}{i_m^2} = \frac{1.2254}{t} \left\{ 1 - \exp \left[ -2.3367 \left( \frac{t}{t_m} \right)^2 \right] \right\} \quad (\text{eq. 7})$$

in which the current,  $i_m$ , and the time,  $t_m$ , correspond to the maximum current of

chronoamperograms. Fig. 3 depicts the non-dimensional theoretical and experimental  $i^2/i_m^2$  versus  $t/t_m$  curves for Watts solutions with and without the addition of different concentrations of  $\text{TiO}_2$  sol, under the deposition potentials of -800 and -900 mV vs. SCE. Fig. 3(a) indicates that at -800 mV vs. SCE, the nickel nucleation in the Ni- $\text{TiO}_2$  nanocomposite matrix follows the progressive mechanism with three-dimensional growth, similar to the pure nickel deposition at a low overpotentials, regardless of the  $\text{TiO}_2$  sol concentration in the solution. In other words, the  $\text{TiO}_2$  particles facilitate the deposition of the Ni ions, but they do not modify the nucleation mechanism of the deposits. Fig. 3(b) shows that under the potential of -900 mV vs. SCE, the nucleation processes of the Ni and Ni- $\text{TiO}_2$  deposits obey an instantaneous mechanism with diffusion-controlled growth, in which the rate of new nuclei formation at the initial time of deposition is significant and all of the nucleation sites become active immediately. The transition from progressive to instantaneous nucleation can be explained by taking into account that at the cathodic potential of -800 mV vs. SCE, the applied overpotential for the nucleation of the nickel deposits is low. Thus, the rate of new nuclei formation proceeds during the longer periods of time, and the progressive nucleation that corresponds to the fast growth of nuclei all activated during the course of the electroreduction occurs. However, at the cathodic potential of -900 mV vs. SCE, the nickel nucleation rate is high and there are many active and preferential sites on the electrode surface for the nucleation of the nickel. On the other hand, higher amounts of  $\text{TiO}_2$  nanoparticles are absorbed on the cathode's surface, and since these particles act as favorable sites for the nucleation of the Ni

deposit, they accelerate the nucleation rate. This leads to the instantaneous nucleation process. The experimental results obtained for the deposition of the Ni- $\text{TiO}_2$  nanocomposites are in agreement with the work of other researchers investigating the influence of deposition potential on the nucleation mechanism of pure nickel [35, 37]. Moreover, via the Scharifker-Hills model, it is demonstrated that under a constant deposition potential, the non-dimensional curves of nickel codeposition with the  $\text{TiO}_2$  particles are similar to those of pure nickel deposition. Although the presence of  $\text{TiO}_2$  nanoparticles shortens the nucleation time, it does not affect the nucleation mechanism of the nickel. In fact, at -800 and -900 mV vs. SCE, the nickel nucleation in both the pure Ni deposits and Ni- $\text{TiO}_2$  nanocomposites displays similar trends and follows progressive and instantaneous mechanisms, respectively, regardless of the presence of  $\text{TiO}_2$  sol in the Watts bath.

In order to confirm the results displayed in Figs. 3 (a) and (b), the  $i-t^{3/2}$  and  $i-t^{1/2}$  curves were plotted at the initial times of the chronoamperograms. According to Equations (8) and (9),  $i-t^{3/2}$  and  $i-t^{1/2}$  exhibit linear dependences for progressive and instantaneous nucleation, respectively [30].

$$J = \frac{zFD^2c}{\pi^{1/2} t^{1/2}} [1 - \exp(-AN\pi k'Dt^2/2)] \quad (\text{eq. 8})$$

$$J = \frac{zFD^2c}{\pi^{1/2} t^{1/2}} [1 - \exp(-N\pi kDt)] \quad (\text{eq. 9})$$

where

$$K^2 = 4/3 (8\pi cM/\rho)^{1/2} \quad \text{and} \quad K = (8\pi cM/\rho)^{1/2}$$

The variable  $zF$  represents the molar charge of the electrodeposited species,  $D$  is the diffusion coefficient,  $c$  is the molar concentration of the metal ions,  $M$  is the molar mass,  $\rho$  is the density

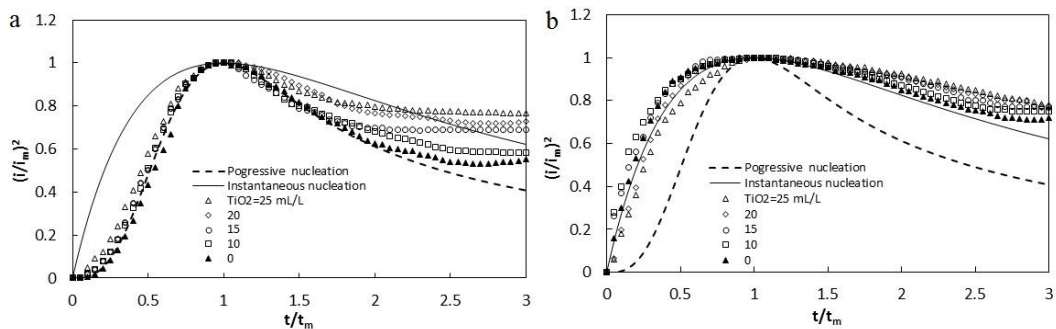


Fig. 3- Non-dimensional  $(i/i_m)^2$  vs.  $t/t_m$  curves corresponding to Fig.2, under the potentials of (a) -800 and (b) -900 mV vs. SCE, for deposition of the Ni and Ni- $\text{TiO}_2$  nanocomposites. Theoretical plots for the progressive and instantaneous nucleations are depicted by the dashed and solid lines, respectively.

of the metal,  $N$  is the number of nucleation sites at time  $t$ , and  $A$  is the constant of the nucleation rate. Fig. 4(a) indicates the linear relationship between  $i$  and  $t^{3/2}$  at  $-800$  mV vs. SCE for different  $\text{TiO}_2$  sol concentrations, which proves conformity with the Scharifker-Hill model for progressive nucleation. However, the  $i-t^{1/2}$  plots at  $-800$  mV vs. SCE in Figure 4(b) have poor linearity compared to the  $i-t^{3/2}$  plots in Fig. 4(a). Figs. 4(c) and (d) illustrate that at a more cathodic deposition potential ( $-900$  mV vs. SCE), the  $i-t^{3/2}$  plots display non-linear behavior, whereas the  $i-t^{1/2}$  plots exhibit linear trends, confirming the instantaneous nucleation mechanism.

The calculations of the nucleation rate ( $AN_0$ ) for the progressive nucleation and the nucleus density ( $N_0$ ) for the instantaneous nucleation were performed according to the following equations:

$$AN_0 = 0.2898 \left( \frac{8\pi cM}{\rho} \right)^{-1/2} \left[ \frac{zFc}{i_{\max}^2 t_{\max}^3} \right]^2 \quad (\text{eq. 10})$$

$$N_0 = 0.0652 \left( \frac{8\pi cM}{\rho} \right)^{-1/2} \left[ \frac{zFc}{i_{\max} t_{\max}} \right]^2 \quad (\text{eq. 11})$$

Data on the progressive and instantaneous nucleation sites are presented in Table 2, as a function of the  $\text{TiO}_2$  sol concentration and deposition potential. It can be observed that

the nucleation rate and number of nucleation sites increase with an increase in the  $\text{TiO}_2$  sol concentration. However, the variation of  $t_m$  with the  $\text{TiO}_2$  content at a constant potential is slight but for a fixed  $\text{TiO}_2$  content, as the potential shifts from  $-800$  to  $-900$  mV vs. SCE, the critical time declines notably thereby increasing the rate of new nuclei formation to a greater extent. Since the initial nickel nucleation on a large number of active sites confines their subsequent availability, the growth of the deposits is restricted to the primitively-formed nuclei. This behavior conforms to the instantaneous nucleation discussed above.

Fig. 5 illustrates the X-ray diffraction phase analysis and TEM image for the  $\text{TiO}_2$  nanoparticles separated from the Ni- $\text{TiO}_2$  composite coatings; these coatings were deposited from the bath containing 25 m/L  $\text{TiO}_2$  sol, under the potential  $-900$  mV vs. SCE, after being annealed at  $450^\circ\text{C}$  for 3 hours. As can be seen in Fig. 5(a), the separated  $\text{TiO}_2$  particles have a crystalline structure, indicating diffraction peaks at  $2\theta = 25.25^\circ$ ,  $37.82^\circ$ , and  $48.21^\circ$ , which are attributed to the (101), (004), and (200) crystal planes of the anatase phase, respectively. These peaks are in good agreement with the standard spectrum (JCPDS no. 21-1272). The diffraction peaks of the rutile or brookite phases

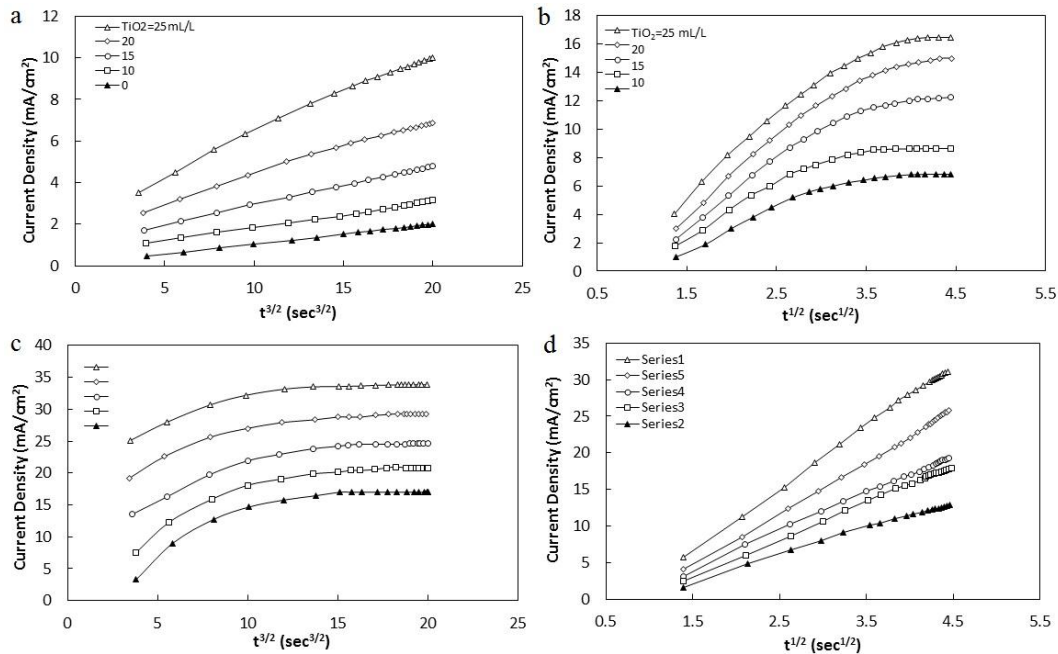


Fig. 4- Plots of (a)  $i-t^{3/2}$  and (b)  $i-t^{1/2}$  from the initial transients in Fig. 2(c), and (c)  $i-t^{3/2}$  and (d)  $i-t^{1/2}$  from the initial transients in Fig. 2(d) for the Ni and Ni- $\text{TiO}_2$  depositions, in order to confirm the progressive and instantaneous nucleation mechanisms, respectively.

Table 2- Nucleation rate and density calculated from the chronoamperograms in Figs. 2(c) and (d)

TiO <sub>2</sub> sol concentration (mL/L)	Potential: -800 mV			Potential: -900 mV		
	t <sub>max</sub> (sec)	i <sub>max</sub> (mA/cm <sup>2</sup> )	AN <sub>0</sub> /10 <sup>5</sup> (cm <sup>-2</sup> s <sup>-1</sup> )	t <sub>max</sub> (sec)	i <sub>max</sub> (mA/cm <sup>2</sup> )	N <sub>0</sub> /10 <sup>5</sup> (cm <sup>-2</sup> )
0	41.113	10.93	3.715	21.273	18.06	5.084
10	38.023	11.51	3.923	17.12	21.52	5.527
15	29.141	13.54	4.818	15.921	25.01	6.087
20	24.252	15.36	5.407	11.224	30.05	6.599
25	19.622	16.24	7.388	9.041	34.13	7.88

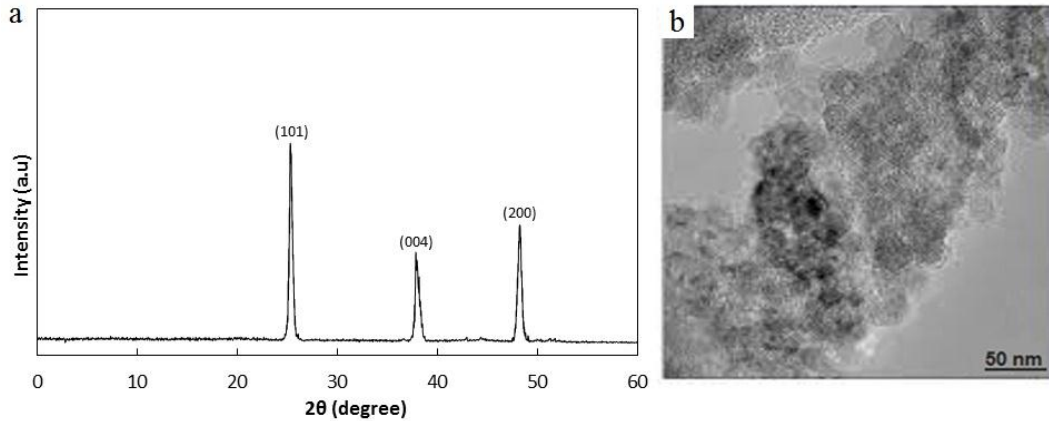


Fig. 5- (a) X-ray diffraction phase analysis, and (b) TEM image of the TiO<sub>2</sub> particles separated from the Ni-TiO<sub>2</sub> composite coating deposited from the bath containing 25 mL TiO<sub>2</sub> sol, under potential -900 mV vs. SCE, after being annealed at 450°C for 3 hours.

do not appear in the phase analysis because of the relatively low temperature of the heat treatment [38]. As depicted in Fig. 5(b), the TiO<sub>2</sub> crystalline particles in the anatase phase have a spherical morphology on a nanometric scale; their grain size can be estimated at about 20 nm.

Fig. 6 demonstrates the relationship between the content of the codeposited TiO<sub>2</sub> particles measured by the experimental method explained above, versus the concentration of TiO<sub>2</sub> sol at the potentials of -800 and -900 mV vs. SCE. The electrodeposition of each coating was repeated 3 times, and the weight percentages of the TiO<sub>2</sub> nanoparticles were analyzed by the standard deviation equation [39]. According to Fig. 6, the codeposition of the Ni-TiO<sub>2</sub> coating is dependent on the TiO<sub>2</sub> sol concentration; as the concentration of the TiO<sub>2</sub> sol in the suspension rises, the amount of embedded TiO<sub>2</sub> particles increases. The addition of low concentrations of TiO<sub>2</sub> sol leads to a rapid increase in particle content, while a large amount of sol results in a slow increase in TiO<sub>2</sub> content, approaching the saturation state. When a small amount of sol solution is added to the Watts bath, the sol is destabilized by hydrated nickel ions in the solution and it is condensed. Afterwards, hydrous nanoparticles are produced and dispersed

by stirring. It has been reported that at pH= 4.2, TiO<sub>2</sub> nanoparticles possess negative surface charge density in the presence of SDS [40]. The negative surface charge is advantageous in the adsorption of Ni<sup>2+</sup> ions; therefore, they can adsorb on the cathode [41]. The electrochemical codeposition consists of electrophoresis (physical) and adsorption (electrochemical). First, the nanoparticles approach the cathode and loosely adsorb on it. These loosely-adsorbed particles are surrounded by a cloud of adsorbed ions. Then, they lose the ionic cloud and strongly adsorb on the cathode. Finally, these strongly-adsorbed particles are trapped by the growing nickel layer [42, 43]. When the concentration of TiO<sub>2</sub> sol is lower than 15 mL/L, an increase in the sol concentration leads to more negative charge being provided; thus, the amount of adsorbed Ni<sup>2+</sup> ions on the surface of the TiO<sub>2</sub> particles increases. The TiO<sub>2</sub> particles are carried with the Ni<sup>2+</sup> ions toward the cathode upon which they can deposit. Therefore, higher concentrations of TiO<sub>2</sub> sol in the bath increase the amount of encapsulated TiO<sub>2</sub> particles in the nickel deposit [44]. On the other hand, for sol concentrations higher than 15 mL/L, more loosely-adsorbed particles are detached from the cathode surface due to agitation, leading to a slower increase in the

particle content of the coatings. Fig. 6 demonstrates that as the deposition potential shifts toward more cathodic values, the  $\text{Ni}^{2+}$  ions gain more positive charge, and as they adsorb more tightly to the  $\text{TiO}_2$  particles, the weight percentages of the codeposited  $\text{TiO}_2$  particles increase as well.

Research related to the traditional electrodeposition of Ni- $\text{TiO}_2$  composite coatings has demonstrated that the codeposition percentage of titania nanoparticles is difficult to quantitatively control, because the particles are frequently agglomerated in the metal matrix, as well as in the electrolyte, due to their significantly high surface energy [10]. However, by adding the  $\text{TiO}_2$  sol to the Watts bath, the hydrous  $\text{TiO}_2$  nanoparticles are easily dispersed by stirring, facilitating the adsorption of the  $\text{Ni}^{2+}$  ions on their surface. As the current passes through the solution, the hydrous  $\text{TiO}_2$  nanoparticles and the  $\text{Ni}^{2+}$  ions are simultaneously transported to the cathode surface under the effect of the electrical field, leading to a higher incorporation of the  $\text{TiO}_2$  nanoparticles in the growing metal matrix [33]. It is noteworthy

that the maximum incorporation percentage of the nanoparticles in the sol-enhanced Ni- $\text{TiO}_2$  nanocomposite coatings achieved at -900 mV is 6.23 wt.% (see Fig. 6), whereas the highest amount of titania embedded particles reported in the literature does not exceed  $\sim 3.5$  wt.% under the same deposition potential [23].

Figs. 7 (a) and (b) show, respectively, the X-ray diffraction patterns of the Ni coating without the addition of  $\text{TiO}_2$  sol to the bath, and Ni- $\text{TiO}_2$  coatings for various concentrations of  $\text{TiO}_2$  sol deposited under the potentials of -800 and -900 mV vs. SCE. The XRD patterns of the pure Ni coating and Ni- $\text{TiO}_2$  nanocomposites show strong peaks at  $2\theta = 44.5^\circ$ , revealing the preferential orientation of the Ni growth along the (111) plane, due to a lower strain in this direction [45]. Other diffraction peaks correspond to the (200), (220), and (311) crystalline planes in the face-centered cubic lattice of Ni (JCPDS no. 45-1027). It should be noted that the peaks at  $2\theta=25.25^\circ$  are assigned to the (101) plane of the anatase (JCPDS no. 21-1272), confirming that  $\text{TiO}_2$  nanoparticles become crystallized after 3 hours of heat treatment at  $450^\circ\text{C}$ . As the concentration of the  $\text{TiO}_2$  sol and the deposition potential increase, the intensity of the peaks corresponding to the anatase phase increases and the growth of Ni along the (220) plane intensifies. However, for the higher concentrations of  $\text{TiO}_2$  sol and under the more cathodic potentials, there is an increase in the content of the codeposited particles that are distributed on the grain boundaries of the Ni. These particles confine the growth of the Ni grains, and decrease the mean sizes of the nickel crystallites in the Ni- $\text{TiO}_2$  coatings. Therefore, the Ni diffraction peak width at half-maximum intensity becomes broader than that of the pure

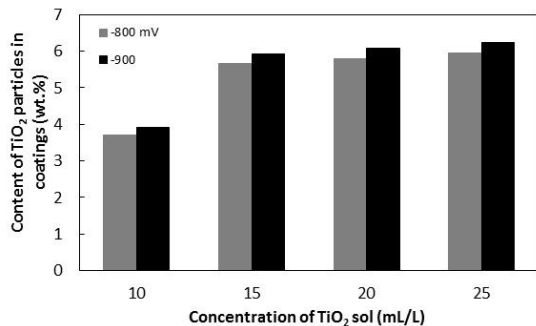


Fig. 6- Variations in  $\text{TiO}_2$  particles' content in the Ni- $\text{TiO}_2$  composite coatings versus different concentrations of  $\text{TiO}_2$  sol deposited under the potentials of -800 and -900 mV vs. SCE.

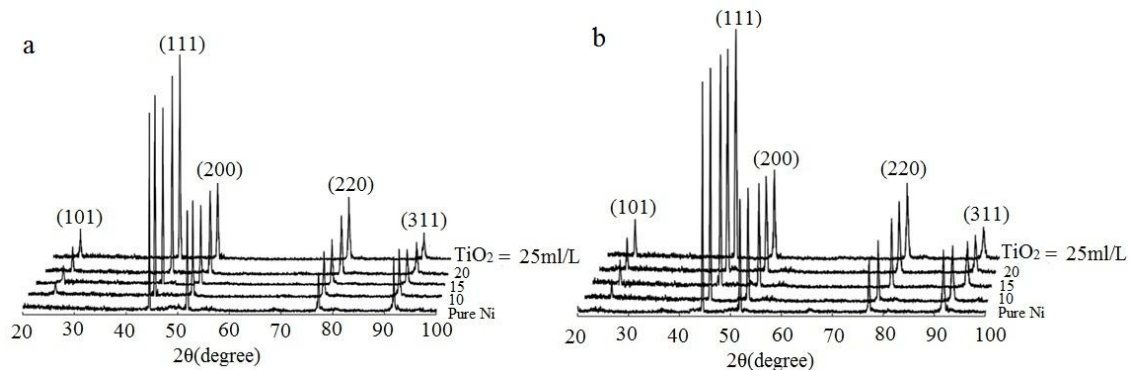


Fig. 7- X-ray diffraction pattern of the pure Ni and Ni- $\text{TiO}_2$  coatings for various concentrations of  $\text{TiO}_2$  sol deposited under the potentials of (a) -800 and (b) -900 mV vs. SCE, after being annealed at  $450^\circ\text{C}$  for 3 hours.

nickel [42]. Table 3 represents the average crystallite sizes of the Ni and Ni-TiO<sub>2</sub> coatings calculated by the Scherrer equation [46]:

$$D = \frac{0.9 \lambda}{B \cos \theta} \quad (\text{eq. 12})$$

where D is the crystallite size, λ is the Cu K<sub>α</sub> wavelength, B is the peak width at half-maximum intensity, and θ is the Bragg's angle. According to the results, as the concentration of the TiO<sub>2</sub> sol and the deposition potential increase, the average crystallite sizes of the Ni and Ni-TiO<sub>2</sub> coatings decrease. The crystallites refinement can be attributed to the higher incorporation of titania nanoparticles, which are distributed along the nickel grain boundaries and act as physical barriers restricting the growth rate. According to Table 3, at the conditions under which the highest incorporation of titania nanoparticles is achieved, the mean crystallite size of the sol-enhanced Ni-TiO<sub>2</sub> nanocomposite coatings is approximately 25.36 nm, which is more refined than that of conventional electrodeposited Ni-TiO<sub>2</sub> nanocomposite [47].

The surface morphologies of the Ni coating and Ni-TiO<sub>2</sub> composite coatings are depicted in Fig. 8. It is evident that the surface of the Ni coating contains regular pyramidal crystals, and a compact deposit is obtained. With the addition of 10 mL/L TiO<sub>2</sub> sol in the bath, the TiO<sub>2</sub> nanoparticles precipitate in the grain interfaces of the Ni and impede the grain growth. Thus, the Ni grains transform from pyramidal to semi-spherical and into a collection of diverse sizes, due to differences in growth rate, as shown in Fig. 8(b). The incomplete coverage of the grains of different sizes results in the formation of a less compact structure than that of the pure nickel coating. As the concentration of the TiO<sub>2</sub> sol increases to 25 mL/L, the nickel grain growth

is hindered by a higher percentage of codeposited nanoparticles, and a more refined grain structure with more porosity is obtained (see Fig. 8(c)). Under the deposition potential of -900 mV vs. SCE, due to the instantaneous nucleation, the nucleation rate is high but the growth rate is limited; this leads to the formation of more superfine Ni grains (see Fig. 8(d)). It should be noted that the sol-enhanced nanocomposite coatings have a more refined structure than traditional electroplated coatings [27]. However, Fig. 8 depicts that with the increase of TiO<sub>2</sub> sol concentration and as the deposition potential becomes more negative, more porous coatings are obtained compared to the pure nickel coating. This can be attributed to the higher incorporation of titania nanoparticles, which induces an increase in the number of nucleation sites and accelerates the nucleation rate of the nickel matrix. Moreover, these nanoparticles are distributed along the nickel grain boundaries and act as physical barriers, slowing down the growth rate. Due to the slow growth rate of a large number of new nuclei, the nickel grains do not find sufficient opportunity to cover each other, leading to the formation of a porous structure.

#### 4. Conclusions

A sol-modified electrodeposition technique was utilized to deposit Ni-TiO<sub>2</sub> nanocomposite coatings. The addition of higher concentrations of TiO<sub>2</sub> sol to the Watts bath decreased the onset deposition potential of the Ni<sup>2+</sup> ions. Chronoampermetric analyses showed that the density of the nucleation sites increased with the addition of higher sol concentrations under higher deposition overpotentials, which reflected the role of TiO<sub>2</sub> particles as favorable sites for nickel nucleation. Under -800 and -900 mV vs.

Table 3- Ni crystallite size as a function of the TiO<sub>2</sub> sol concentration and deposition potential

Potential (mV)	TiO <sub>2</sub> sol concentration (mL/L)	Ni crystallite size (nm)				
		(111)	(200)	(220)	(311)	Average
-800	0	65.96	55.20	46.21	38.03	51.35
-800	10	53.59	44.16	33.89	30.02	40.42
-800	15	40.83	35.33	29.05	27.17	33.10
-800	20	37.28	33.97	25.41	24.28	30.24
-800	25	32.12	28.49	22.60	22.82	26.51
-900	0	61.25	53.62	43.47	31.70	47.51
-900	10	47.12	40.14	31.91	28.79	36.99
-900	15	34.72	30.46	27.56	25.33	29.52
-900	20	33.24	29.44	22.84	22.69	27.05
-900	25	32.36	27.61	20.33	21.14	25.36

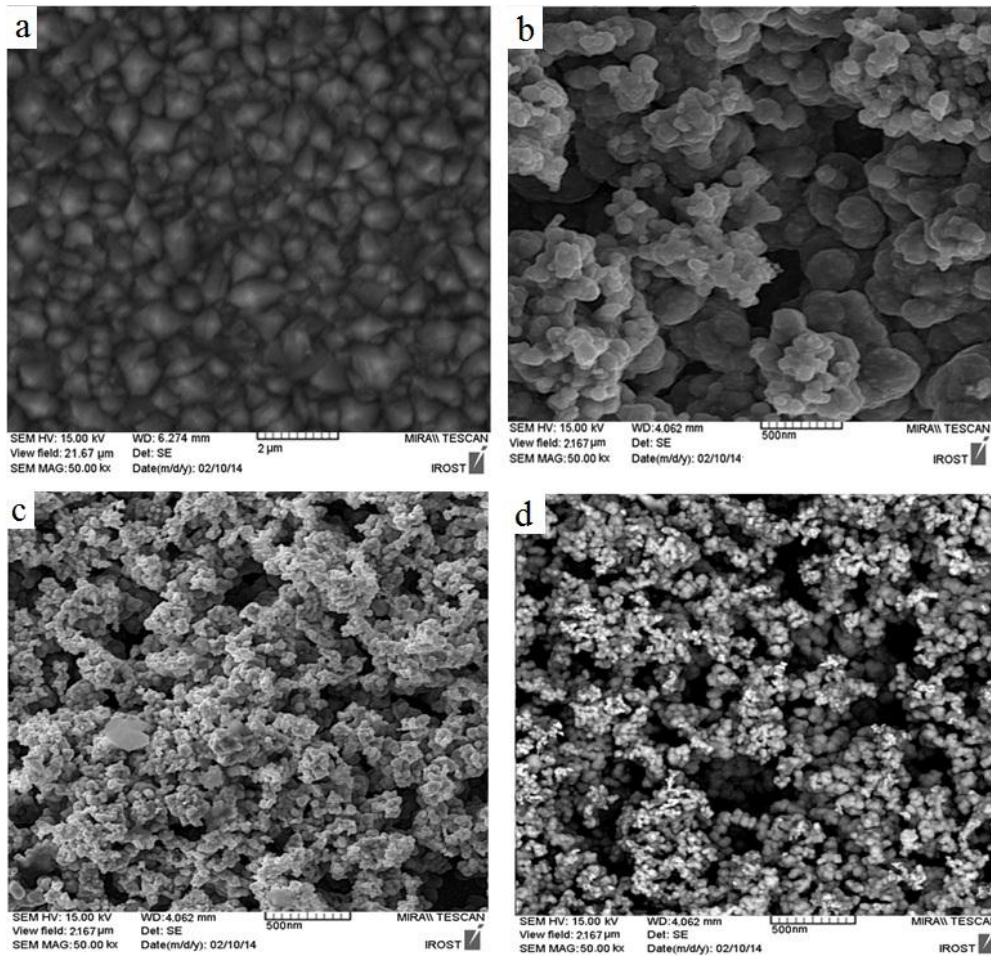


Fig. 8- Scanning electron microscopy (SEM) of (a) pure nickel coating deposited under -800 mV and Ni-TiO<sub>2</sub> composite coatings for various concentrations of TiO<sub>2</sub> sol, deposited under different potentials, (b) 10 mL/L, -800 mV, (c) 25 mL/L, -800 mV, and (d) 25 mL/L, -900 mV.

SCE, regardless of the TiO<sub>2</sub> sol concentration, the electrodeposition of the Ni-TiO<sub>2</sub> nanocomposite followed progressive and instantaneous nucleation mechanisms, respectively, with 3D growth process. Larger amounts of codeposited TiO<sub>2</sub> nanoparticles could be obtained with the addition of higher concentrations of TiO<sub>2</sub> sol under higher overpotentials. After the heat treatment, the TiO<sub>2</sub> nanoparticles (~20 nm) became crystallized in the coating. Higher concentrations of TiO<sub>2</sub> sol did not modify the nucleation mechanism of nickel deposits, but rather refined the Ni crystallites and changed their shape from pyramidal to spherical, especially under high overpotentials.

## References

1. Polushin NI, Kudinov AV, Zhuravlev, VV. Dispersed strengthening of a diamond composite electrochemical coating with nanoparticles. *Russian Journal of Non-Ferrous Metals*. 2013;54:412-416.

2. Kharratian Khameneh S, Heydarzadeh Sohi M, Ataie A. Surfactant-Assisted Electrodeposition of CoFe-Barium Hexaferrite Nanocomposite Thin Films. *Journal of Ultrafine Grained and Nanostructured Materials*. 2014;47:51-56.
3. Jaleh B, Shahbazi N. Surface properties of UV irradiated PC-TiO<sub>2</sub> nanocomposite film. *Applied Surface Science*. 2014;313:251-258.
4. Barzegar Vishlaghi M, Ataie A. Role of Intensive Milling on Microstructural and Physical Properties of Cu<sub>80</sub>Fe<sub>20</sub>/10CNT Nano-Composite. *Journal of Ultrafine Grained and Nanostructured Materials*. 2014;47:37-42.
5. Zandi R, Ershad R, Rahimi A. Silica based organic-inorganic hybrid nanocomposite coatings for corrosion protection. *Progress in Organic Coatings*. 2005;53:286-291.
6. Abolhasani A, Aliofkhaezrai M, Farhadi SS, Sabour Rouhaghdam A, Asgari M. Growth, corrosion, and wear study of nanocomposite PEO coating in electrolyte containing nickel sulfate. *Journal of Ultrafine Grained and Nanostructured Materials*. 2015;48:133-144.
7. Kamali Heidari H, Ataie A, Heydarzadeh Sohi M, Kim JK. Effect of processing parameters on the electrochemical performance of graphene/ nickel ferrite

- (G-NF) nanocomposite. *Journal of Ultrafine Grained and Nanostructured Materials*. 2015;48:27-35.
8. Ho KH, Newman ST. State of the art electrical discharge machining (EDM). *International Journal of Machine Tools and Manufacture*. 2003;43:1287-1300.
  9. Spanou S, Pavlatou EA, Spyrellis N. Ni/nano-TiO<sub>2</sub> composite electrodeposits: Textural and structural modifications. *Electrochimica Acta*. 2009;54:2547-2555.
  10. Chen W, Gao W, He Y. A novel electroless plating of Ni-P-TiO<sub>2</sub> nanocomposite coatings. *Surface and Coatings Technology*. 2010;204:2493-2498.
  11. Simonsen SME, Sogaard EG. Identification of Ti clusters during nucleation and growth of sol-gel derived TiO<sub>2</sub> nanoparticles. *European Journal of Mass Spectrometry*. 2013;19:265-273.
  12. Chen W, Gao W. Sol-enhanced electroplating of nano structured Ni-TiO<sub>2</sub> composite coatings-The effects of sol concentration on the mechanical and corrosion properties. *Electrochimica Acta*. 2010;55:6865-6871.
  13. CHASSAING E, JOUSSELLIN M, WIART RJ. The kinetics of nickel electrodeposition: Inhibition by adsorbed hydrogen and anions. *Journal of Electroanalytical Chemistry*. 1983;157:75-78.
  14. Grujicic D, Pesic B. Electrochemical and AFM study of nickel nucleation mechanisms on vitreous carbon from ammonium sulfate solutions. *Electrochimica Acta*. 2006;51:2678-2690.
  15. Rusu DE, Ispas A, Bund A. Corrosion tests of nickel coatings prepared from a Watts-type bath. *Journal of Coatings Technology and Research*. 2012;9:87-95.
  16. Ispas A, Matsushima H, Bund A. Nucleation and growth of thin nickel layers under the influence of a magnetic field. *Journal of Electroanalytical Chemistry*. 2009;626:174-182.
  17. Nasirpour F, Janjan SM, Peighambari SM. Refinement of electrodeposition mechanism for fabrication of thin nickel films on n-type silicon (111). *Journal of Electroanalytical Chemistry*. 2013;690:136-143.
  18. Yermokhina NI, Bukhtiyarov VK. Nanocomposite Ni/TiO<sub>2</sub>-materials for hydrogen generation systems. *International Journal of Hydrogen Energy*. 2011;36:1364-1368.
  19. Moazeni M, Moradi M, Torkan S, Kermanpur A, Karimzadeh F. The Effect of Process Parameters on the Synthesis of Ti and TiO<sub>2</sub> Nanoparticles Produced by Electromagnetic Levitational Gas Condensation. *Journal of Ultrafine Grained and Nanostructured Materials*. 2012;45:41-45.
  20. He Z, Xiao J, Xia F. Enhanced solar water-splitting performance of TiO<sub>2</sub> nanotube arrays by annealing and quenching. *Applied Surface Science*. 2014;313:633-639.
  21. Kapridaki C, Pinho L, Mosquera MJ. Producing photoactive, transparent and hydrophobic SiO<sub>2</sub> crystalline TiO<sub>2</sub> nanocomposites at ambient conditions with application as self-cleaning coatings. *Applied Catalysis B: Environmental*. 2014;156:416-427.
  22. Perillo PM, Rodriguez DF. A room temperature chloroform sensor using TiO<sub>2</sub> nanotubes. *Sensors and Actuators B: Chemical*. 2014;193:263-266.
  23. Aal AA. Hard and corrosion resistant nanocomposite coating for Al alloy. *Materials Science and Engineering*. 2008;474:181-187.
  24. Spanou S, Kontos AI, siokou A. Self-cleaning behaviour of Ni/nano-TiO<sub>2</sub> metal matrix composites. *Electrochimica Acta*. 2013;105:324-332.
  25. Olya ME, Pirkarami A, Soleimani M. Photoelectrocatalytic degradation of acid dye using Ni-TiO<sub>2</sub> with the energy supplied by solar cell: Mechanism and economical studies. *Journal of Environmental Management*. 2013;121:210-219.
  26. Pirkarami A, Olya ME, Farshid SR. UV/Ni-TiO<sub>2</sub> nanocatalyst for electrochemical removal of dyes considering operating costs. *Water Resources and Industry*. 2014;5:9-20.
  27. Bagheri P, Farzam M, Mousavi AB. Ni-TiO<sub>2</sub> nanocomposite coating with high resistance to corrosion and wear. *Surface and Coatings Technology*. 2010;204:3804-3810.
  28. Lin CS, Lee CY, Chang CF. Annealing behavior of electrodeposited Ni-TiO<sub>2</sub> composite coatings. *Surface and Coatings Technology*. 2006;200:3690-3697.
  29. Cui CQ, Lee JY. Nickel deposition from unbuffered neutral chloride solutions in the presence of oxygen. *Electrochimica Acta*. 1995;40:1653-1662.
  30. Petrovic Z, Hukovic MM, Grubac Z. The nucleation of Ni on carbon microelectrodes and its electrocatalytic activity in hydrogen evolution. *Thin Solid Films*. 2006;513:193-200.
  31. Bard AJ, Faulkner LR. *Electrochemical methods; fundamentals and applications*. 2004; New York:John Wiley & Sons.
  32. Aal EE. Breakdown of passive film on nickel in borate solutions containing halide anions. *Corrosion Science*. 2003;45:759-775.
  33. Whithers JC. *Electrodepositing. Products Finishing*. 1962;26:62-70.
  34. Rezaei M, Ghorbani M, Dolati A. Electrochemical investigation of electrodeposited Fe-Pd alloy thin films. *Electrochimica Acta*. 2010;56:483-490.
  35. Gomez E, Muller C, Proud WG. Electrodeposition of nickel on vitreous carbon: Influence of potential on deposit morphology. *Journal of Applied Electrochemistry*. 1992;22:872-876.
  36. Scharifker BR. Theoretical and experimental studies of multiple nucleations. *Electrochimica Acta*. 1983;28:879-889.
  37. Chengyu T, Yu L. Nickel codeposition with SiC particles at initial stage. *Transactions of Nonferrous Metals Society of China*. 2008;18:1128-1133.
  38. Habibpanah AA, Pourhashem S, Sarpoolaky H. Preparation and characterization of photocatalytic titania-alumina composite membranes by sol-gel methods. *Journal of the European Ceramic Society*. 2011;31:2867-2875.
  39. Miller JN, Miller JC. *Statistics and chemometrics for analytical chemistry*. Great Britain. 2005; Ashford Colour Press.
  40. Chibowski E, Holysz L, Terpilowski K. Influence of ionic surfactants and lecithin on stability of titanium dioxide in aqueous electrolyte solution. *Croatica Chemica Acta*. 2007;80:395-403.
  41. Hovestad A, Janssen LJJ. Electrochemical codeposition of inert particles in a metallic matrix. *Journal of Applied Electrochemistry*. 1995;25:519-527.
  42. Srivastava M, Selvi VE, Grips VKW. Electrochemical deposition and tribological behavior of Ni and Ni-Co metal matrix composites with SiC nanoparticles. *Applied Surface Science*. 2007;253:3814-3824.

43. Thangavel S, Ramaraj R. Electrochemical and in situ spectroelectrochemical studies on the gold nanoparticles co-deposited with cobalt hexacyanoferrate modified electrode and its application in sensor. *Journal of Nanoscience and Nanotechnology*. 2004;9:2353-2363.
44. Vaghefi SM, Saatchi A, Hoseinabadi M. Deposition and properties of electroless Ni-P-B<sub>4</sub>C composite coatings. *Surface and Coatings Technology*. 2003;168:259-262.
45. Kumar K, Kalaigan G, Muralidharan VS. Direct and pulse current electrodeposition of Ni-W-TiO<sub>2</sub> nanocomposite coatings. *Ceramics International*. 2013;39:2827-2834.
46. Cullity BD, Stock SR, Stock S. *Elements of X-ray diffraction*. 2001; London: Addison-Wesley.
47. Aal AA, Hassan HB. Electrodeposited nanocomposite coatings for fuel cell application. *Journal of Alloys and Compounds*. 2009;477:652-656.